Predicting Response to Radioimmunotherapy from the Tumor Microenvironment of Colorectal Carcinomas

Ethaar El Emir,[1] Uzma Qureshi,[1] Jason L.J. Dearling,[1] Geoffrey M. Boxer,[1] Innes Clatworthy,[2] Amos A. Folarin,[1] Mathew P. Robson,[1] Sylvia Nagl,[1] Moritz A. Konerding,[3] and R. Barbara Pedley[1]

Departments of [1]Oncology and [2]Histopathology, University College London (Hampstead Campus), London, United Kingdom and [3]Department of Anatomy, Johannes Gutenberg University, Mainz, Germany

Abstract

Solid tumors have a heterogeneous pathophysiology, which directly affects antibody-targeted therapies. Here, we consider the influence of selected tumor parameters on radioimmunotherapy, by comparing the gross biodistribution, microdistribution, and therapeutic efficacy of either radiolabeled or fluorescently labeled antibodies (A5B7 anti–carcinoembryonic antigen antibody and a nonspecific control) after i.v. injection in two contrasting human colorectal xenografts in MF1 nude mice. The LS174T is moderately/poorly differentiated, whereas SW1222 has a well-differentiated glandular structure. Biodistribution studies (1.8 MBq ^{131}I-labeled A5B7, four mice per group) showed similar gross tumor uptake at 48 h in the two models (25.1% and 24.0% injected dose per gram, respectively). However, in therapy studies (six mice per group), LS174T required a 3-fold increase in dose (18 versus 6 MBq) to equal SW1222 growth inhibition (~55 versus ~60 days, respectively). To investigate the basis of this discrepancy, high-resolution multifluorescence microscopy was used to study antibody localization in relation to tumor parameters (5 min, 1 and 24 h, four mice per time point). Three-dimensional microvascular corrosion casting and transmission electron microscopy showed further structural differences between xenografts. Vascular supply, overall antigen distribution, and tumor structure varied greatly between models, and were principally responsible for major differences in antibody localization and subsequent therapeutic efficacy. The study shows that multiparameter, high-resolution imaging of both therapeutic and tumor microenvironment is required to comprehend complex antibody-tumor interactions, and to determine which tumor regions are being successfully treated. This will inform the design of optimized clinical trials of single and combined agents, and aid individual patient selection for antibody-targeted therapies. [Cancer Res 2007;67(24):11896–905]

Introduction

For over a decade, monoclonal antibodies have been licensed for cancer treatment, and have become established as a major and rapidly expanding area of therapy, increasing the need to understand and optimize the systems for enhanced efficacy. In radioimmunotherapy, antibodies raised against tumor-associated antigens are used to target therapeutic radionuclides selectively to the tumor. This not only reduces systemic toxicity, but gives access to metastatic tumor deposits that may be occult or difficult to treat by external beam radiotherapy (1). In the case of non–Hodgkin's lymphoma, radioimmunotherapy has produced significant responses in relapsed patients and is showing excellent response rates as a frontline therapy (1, 2). However, with the exception of micrometastatic disease (3), and recent promising results using pretargeting and combined strategies (4–6), radioimmunotherapy has reduced efficacy in many common solid tumors such as colorectal adenocarcinoma (7).

Heterogeneity of antibody distribution and tumor pathophysiology are major influences on response to radioimmunotherapy. In previous articles, we have discussed how properties related to the antibody and radionuclide effect on therapeutic outcome, and how these may be optimized for therapy (8–11). We have also shown that radioimmunotherapy can significantly enhance other therapies such as vascular-disrupting agents without increasing toxicity (12–14), and this is currently in clinical trial within our department. The present study, however, investigates how properties of the tumor itself influence radioimmunotherapy, concentrating on the treatment of colorectal adenocarcinoma. The radioresistance of this tumor has frequently been cited as a major cause of treatment failure, but other pathophysiologic factors are likely to play an equally important role. A major problem is the abnormality of tumor blood vessels, which frequently leads to a heterogeneous distribution of antibody throughout the tumor and renders some areas inaccessible. On the positive side, their hyperpermeability allows antibody to extravasate more readily from tumor vessels than those of normal tissues (15, 16).

In the current work, we consider the influence of three major parameters on radioimmunotherapy: antigen distribution, vascular supply, and tumor structure. This was achieved by comparing gross biodistribution, microdistribution, and therapeutic efficacy of either radiolabeled or fluorescently labeled antibodies [anti–carcinoembryonic antigen (CEA) antibody and a nonspecific control] in two morphologically distinct colorectal tumor models in nude mice, selected to illustrate typical clinical scenarios. The major differences in blood vessel distribution and architecture between these two models, LS174T and SW1222, were shown in two dimension by fluorescence images of tumor sections, and confirmed for the whole tumors using three-dimensional vascular corrosion cast techniques followed by scanning electron microscopy and X-ray micro–computed tomography (micro-CT). To see whether additional factors were impeding antibody motility through the tumor, we used transmission electron microscopy to compare structure, with particular emphasis on the presence and distribution of gap junctions.

The present study indicates that the pattern of antigen distribution throughout the tumor was of major importance in

Requests for reprints: R. Barbara Pedley, Department of Oncology, University College London, Rowland Hill Street, London NW3 2XR, United Kingdom. Phone: 44-20-7472-6303; E-mail: r.b.pedley@ucl.ac.uk.

doi:10.1158/0008-5472.CAN-07-2967

antibody-targeted therapy, interrelated with vessel distribution and tumor structure. Interstitial pressure and the presence of gap junctions did not seem to significantly affect antibody motility in these models, although the large intercellular gaps between SW1222 cells almost certainly enhanced the rate of movement. Our results show that multiparameter, high-resolution imaging of both therapeutic and tumor microenvironment is required to fully understand the complex nature of the antibody-tumor interaction, and determine which regions are being successfully treated. This informs the design of improved targeting molecules and selection of the most suitable combined therapies for optimized clinical trials.

Materials and Methods

Xenografts. Two human colorectal adenocarcinoma cell lines, LS174T and SW1222 (13), were used to develop xenograft models in the flanks of female nude MF1 mice, 2 to 3 months of age and weighing 20 to 25 g. Subsequent passaging was by s.c. implantation of small tumor pieces ($\sim$1.0 mm^3). The two models had a similar range of CEA expression (22–70 μg/g tumor) but neither secreted measurable antigen into the circulation. All experiments were in compliance with the United Kingdom Coordinating Committee on Cancer Research Guidelines for the Welfare of Animals in Experimental Neoplasia.

Xenograft morphology by bright-field microscopy. Formalin-fixed, paraffin-embedded tumors were sectioned at 5 μm, and comparative morphology of the two xenografts was shown by H&E staining. To study antigen distribution, the sections were stained with anti-CEA antibody as previously described (17) and counterstained with hematoxylin.

Three-dimensional microvascular architecture of xenografts by corrosion casting. Detailed vascular development of the two models was investigated by preparing microvascular corrosion casts, using Mercox CL-2B (Vilene Med. Co.) diluted with 20% methylmethacrylate monomers (Merck) as a casting medium, as previously described (18). Three-dimensional tumor images were reconstructed using the ESEM XL 30 scanning electron microscope (FEI). In addition, three-dimensional reconstructions were done using X-ray high-resolution micro-CT (SkyScan 1172).

Transmission electron microscopy studies. Transmission electron microscopy (TEM) was used to compare detailed morphology of the two xenografts and normal mouse colon. In brief, tissues were prepared as follows: pieces of tissue <2 mm^3 were fixed in 1.5% paraformaldehyde/1.5% glutaraldehyde in phosphate buffer for 2 h and postfixed in 1.0% osmium tetroxide/1.5% ferricyanide for 2 h, followed by dehydration in graded alcohols and embedded in Lemix epoxy resin (TAAB Laboratories Equipment Ltd.). Ultrathin sections (60–90 nm) were stained with uranyl acetate and Reynold's lead citrate. Sections were viewed on a Philips CM120 transmission electron microscope (FEI UK Ltd.).

Antibody studies. A5B7, a monoclonal anti-CEA antibody (12), was used for both distribution and therapy studies. This antibody and its fragments are in regular preclinical and clinical use, and have shown efficacy in radioimmunotherapy and combined antivascular studies within our department (7, 12, 19, 20). The isotype-matched IgG MOPC-31c (MOPC), produced by the mineral oil–induced plasmocytoma MOPC-31c, was used as a nonspecific control, as in previous experiments (8).

Antibody radiolabeling. A5B7 and MOPC were labeled with ^{131}I using the chloramine-T method to a specific activity of either 60 MBq/0.5 mg protein or 180 MBq/0.5 mg protein (12). The antibodies were then used for biodistribution (gross tissue counts) and therapy studies (tumor growth) in the two models.

Biodistribution studies with radiolabeled antibody. Both ^{131}I-labeled A5B7 and MOPC (1.8 MBq/5.0 μg in 0.1 mL PBS) were administered into the tail vein of two groups of four mice bearing either LS174T or SW1222 size-matched xenografts ($\sim$0.5 cm^3). Animals were bled at 48 h, then liver, kidney, lung, spleen, colon, muscle, and tumor were removed for comparative activity assessment by gamma counter (Wizard; Pharmacia). Results were expressed as percentage injected dose per gram of tissue (%ID/g).

Therapy studies with radiolabeled antibody. Experiments commenced when xenografts reached $\sim$0.2 cm^3. Groups of six mice bearing LS174T or SW1222 tumors were given either 6 MBq/50 μg or 18 MBq/50 μg ^{131}I-A5B7 i.v. Control groups received the same doses of nonspecific antibody or no treatment. Tumors were measured twice weekly until volume (length $\times$ width $\times$ height/2) reached 2.0 cm^3 and the mice were sacrificed (21). Mice were given food and water *ad libitum*; the water contained 0.1% potassium iodide to block thyroid uptake of iodine. Weights were taken twice weekly to assess treatment toxicity.

Phosphor plate image analysis studies with radiolabeled antibody. Distribution of radiolabeled-specific and nonspecific antibodies across whole LS174T tumor sections over time was investigated by phosphor plate image analysis at 3, 24, and 48 h post injection, using four mice per group (1.8 MBq/5.0 μg per mouse), as previously described (22–24). Sections were subsequently stained with H&E, and the two images were registered using the cross-correlation method (22). Antibody distribution was quantified in relation to morphology by drawing regions of interest around viable and necrotic areas, and calculating mean pixel values for each over time (23, 24).

Fluorescence labeling of antibody. A5B7 or MOPC (2 mg/mL) was labeled using Alexa Fluor 546 Protein Labeling Kit (Invitrogen), according to the manufacturer's instructions.

Biodistribution studies with fluorescently labeled antibody. The antibody (100 μg) was administered into the tail vein of nude mice bearing either LS174T or SW1222 tumors, and groups of four mice were culled at 5 min, 1 h, and 24 h. The perfusion marker Hoechst 33342 (Invitrogen) was injected i.v. 1 min before killing (10 mg/kg). Tumors were removed, snap frozen in isopentane, and stored at −80°C. Following sectioning at 10 μm, the relevant incubations were done to investigate microdistribution of fluorescently labeled antibody in relation to the following tumor parameters: perfusion, blood vessel distribution (anti-CD31), and CEA distribution, as previously described (13, 14, 25, 26). Each section was viewed under UV, FITC, and rhodamine filters using an Axioskop 2 microscope (Carl Zeiss Ltd.) fitted with a computer-controlled motorized stage, and captured by an AxioCam digital camera with KS300 image analysis software (Carl Zeiss; refs. 13, 14). The three fluorescence images were coregistered to show the interrelationship of antibody and tumor biology. Individual microscope fields were either viewed alone or montaged to form digital images of larger areas or complete tumor sections. Sections were subsequently stained with H&E to compare fluorescence images with corresponding morphology.

Quantitation of fluorescently labeled antibody movement over time. Antibody distance from the nearest perfused vessel was measured at 1 and 24 h using ER Mapper and ER Viewer software on the fluorescence images. Data were collected from groups of four mice per model at each time point, using four fluorescence images per mouse ($\times$20 images; $\sim$300 measurements per image).

Statistics. For biodistribution studies, treatment groups were compared using the Mann-Whitney *U* test. Survival of therapy groups was compared according to the Lee and Desu statistic (27). "Significant" in the text indicates a *P* value of <0.05.

Results

Xenograft morphology by bright-field microscopy. The morphology of LS174T (Fig. 1*A*) showed a moderate to poorly differentiated tumor with little glandular differentiation, and with a heterogeneous blood supply. The CEA was also distributed heterogeneously throughout the tumor, with greatest expression on perivascular tumor cells (Fig. 1*B*). The SW1222 xenograft, however, was organized into polarized well-defined glands, composed of columnar-shaped cells around a central lumen, most glands being surrounded by blood vessels (Fig. 1*C*). Wide intercellular spaces were observed between tumor cells. CEA expression was mainly restricted to the luminal surface of cells surrounding each gland (Fig. 1*D*), reminiscent of antigen distribution in normal colon. Therefore, the morphology, antigen, and blood vessels presented a

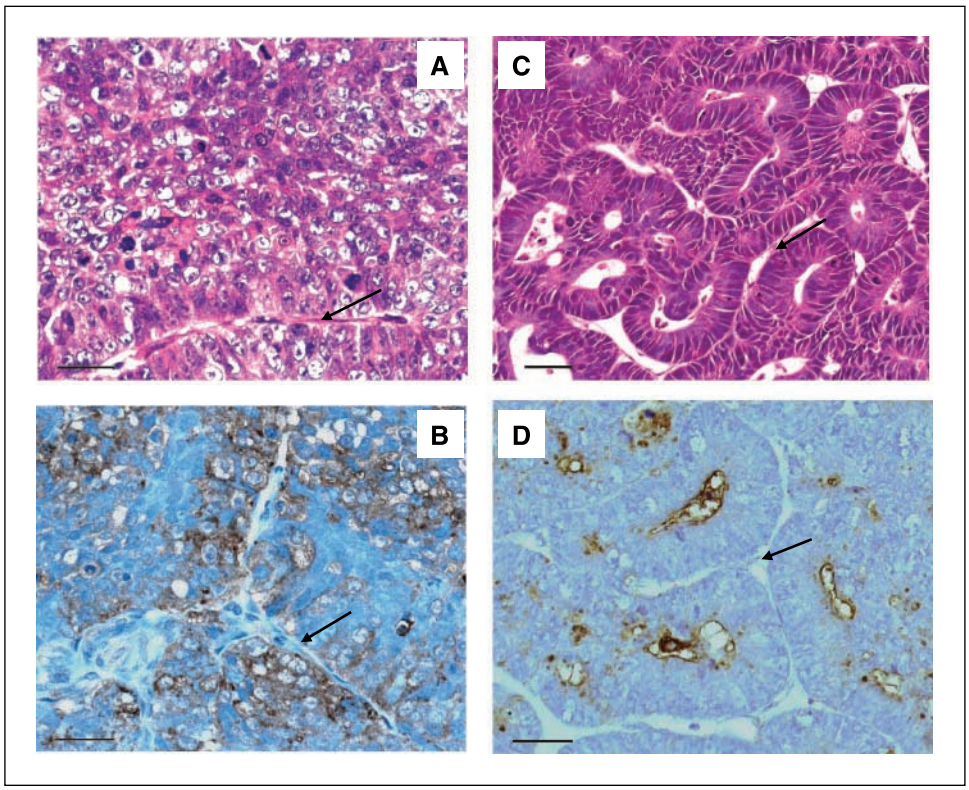

Figure 1. Sections of LS174T and SW1222 colorectal xenografts. *A* and *C,* histologic appearance (H&E) of LS174T showing a poorly differentiated tumor with heterogeneous distribution of blood vessels (*A*), and SW1222 showing a well-differentiated tumor with regular blood vessels around glands (*C*). *B* and *D,* CEA distribution on perivascular tumor cells in LS174T (*B*) and on the luminal surface of tumor cells in SW1222 (*D*). Magnification, ×40. *Arrows,* blood vessels. *Bars,* 50 μm.

far more homogeneous pattern throughout the tumor mass than seen in LS174T (12, 13).

Three-dimensional microvascular architecture of xenografts by corrosion casting. A comparison of three-dimensional microvascular corrosion casts from the two models clearly showed major differences in vessel structure, density, and distribution (Fig. 2). Representative images of whole tumors, obtained as volume renderings from the micro-CT data, show that LS174T had fewer vessels, with a more chaotic and heterogeneous distribution, than the SW1222 (Fig. 2*A* and *C*, respectively), reflecting results from bright-field microscopy. Details of these differences are shown in the high-power scanning electron microscopy images; the vessels in LS174T (Fig. 2*B*) showed a greater lack of hierarchy, with larger intervessel distances and more blind ends than SW1222 (Fig. 2*D*). Although both tumors exhibited a distinctly abnormal vasculature compared with normal colon (17), in SW1222 this had a more homogeneous distribution and regular pattern than in LS174T (Fig. 2*B* and *D*).

Transmission electron microscopy. Detailed structure of the two tumors was compared both with each other and with normal mouse colon, using TEM (Fig. 3). Normal colon showed regularly shaped epithelial cells lined up along the lumen, with small intercellular gaps and regular connecting gap junctions (Fig. 3*A*). However, the cells forming the LS174T xenograft were randomly scattered throughout the tumor in a compact manner, and whereas the intercellular spaces showed variation in width, they had a tendency to be fairly narrow and resemble those of normal colon. Gap junctions were frequently observed between closely opposed cells throughout the tumor (Fig. 3*B*). SW1222 was superficially more similar to normal colon, with regular sized and shaped cells forming relatively structured glands between blood vessels and central lumen. However, a unique feature was the presence of large intercellular spaces (Figs. 1*C* and 3*C*). Gap junctions were seen where membranes of adjacent cells forming the glands came into close contact, but were shorter, and seemed to be less frequent, than in normal colon or LS174T.

Biodistribution studies with radiolabeled antibody. At 48 h post A5B7, there was no significant difference ($P > 0.05$) in %ID/g of tumor and normal tissues between mice bearing either xenograft (Fig. 4*A* and *B*). The antibody showed good tumor selectivity, with 25.1% (SD 3.1%) and 24.0% (SD 3.5%) for LS174T and SW1222, respectively, and tumor to blood ratios of 3.9:1 and 4.2:1. Comparative data for MOPC at 48 h was 1.45% (SD 0.6%), with a tumor to blood ratio of 0.67:1 (not shown).

Therapy studies with radiolabeled antibody. Figure 4*C* and *D* shows mean tumor growth for the two models over time following radioimmunotherapy, demonstrating that LS174T required a 3-fold increase in dose (18.0 versus 6.0 MBq) to equal the growth inhibition seen in SW1222. In LS174T, a dose of 6.0 MBq ^{131}I-labeled A5B7 had no effect on subsequent tumor growth compared with untreated controls ($P > 0.05$, not shown), whereas a dose of 18.0 MBq produced significant inhibition of ~55 days. In SW1222, a dose of 6.0 MBq did produce significant growth inhibition (~60 days), whereas 18.0 MBq totally eradicated the tumor, with no regrowth until the experiment was terminated at 6 months. The nonspecific antibody produced no significant growth delay in LS174T or SW1222 at either dose ($P > 0.05$, not shown). No significant weight loss was seen following any treatment.

Microdistribution of fluorescently labeled antibody in LS174T tumors. A detailed study of A5B7 movement over time (Fig. 5*A*) showed that, as early as 5 min post i.v. injection, the antibody was extravasating from perfused vessels and entering the tumor. By 1 h, the antibody had bound to antigen on perivascular tumor cells, where it was retained at 24 h.

Microdistribution of fluorescently labeled antibody in SW1222 tumors. Again, A5B7 was extravasating by 5 min post-administration, but in this case could already be seen moving through the large gaps between tumor cells (Fig. 5*B*). Unlike LS174T, the antibody diffused rapidly away from vessels and through the tumor mass, and by 1 h was bound to antigen on the luminal surface of tumor glands, between perfused vessels (Fig. 5*B*), where it was still observed at 24 h.

Prolonged retention of antibody at the respective antigen sites is shown by high-power images of LS174T and SW1222 at 24 h post injection (Fig. 5*C*).

Antigen-antibody interaction. The specific binding of antibody to CEA in both models was confirmed by staining for antigen (*green*) and observing fluorescently labeled antibody distribution (*red*) within the same tumor section at 1 h after administration (Fig. 5*D*). LS174T showed colocalization (*yellow*) on perivascular tumor cells, but free antigen was clearly visible away from the vessels. Conversely, in SW1222, colocalization was already seen on the luminal surface of well-defined glands, away from the blood vessels, with most antigen associated with bound antibody. Antigen distribution for both tumors reflected immunohistochemical data (Fig. 1*B* and *D*).

The importance of antibody-antigen interaction on A5B7 distribution throughout the tumor was investigated by montaging individual multifluorescence images into whole tumor sections at 1 and 24 h post antibody (Fig. 6*A* and *B*). Subsequent H&E staining of the same sections showed that both xenografts were mainly viable, with LS174T containing some central necrosis. In LS174T, the A5B7 has clearly localized to antigen on perivascular tumor cells at both time points. Overall, the antibody had an extremely heterogeneous and patchy distribution (Fig. 6*A*), with concentration at the periphery and large areas of tumor remaining untargeted. However, in SW1222, the regular distribution of antigen and blood vessels produced a far more homogeneous antibody distribution throughout the tumor at 1 h, and increasingly at 24 h after antibody injection (Fig. 6*B*). Calculated on a pixel-by-pixel basis at 24 h, 7.2% and 12.8% of the tumor images were composed of antibody for LS174T and SW1222, respectively, demonstrating more uniform targeting in the latter. The two-dimensional fluorescence images of vessel distribution in both tumors closely resembled their three-dimensional vascular casts (Fig. 2*A* and *C*).

Quantitation of fluorescently labeled antibody movement over time. Antibody movement away from perfused vessels and through the tumor mass was quantified for both models, using high-resolution images (Fig. 6*C* and *D*). At 1 h, the antibody in LS174T was bound to antigen on perivascular tumor cells, the majority lying within 20 to 30 μm distance with a peak at 10 to 20 μm (1–2 cell diameters). The same peak was seen at 24 h, with slight diffusion across the tumor (Fig. 6*C*). The SW1222 xenograft showed greater antibody dispersal; it had clearly moved away from vessels by 1 h, and bound to antigen on tumor cells surrounding the nearest glandular lumen, with a peak at 30 to 40 μm (Fig. 6*D*). By 24 h, the antibody was still retained in these glands, but had also reached further glands, with a peak at 40 to 50 μm. The small proportion of antibody at a distance from the vasculature in both tumors was probably associated with out-of-field vessels. Data from both models reflected the whole tumor images of antibody distribution (Fig. 6*A* and *B*). Fluorescently labeled MOPC was

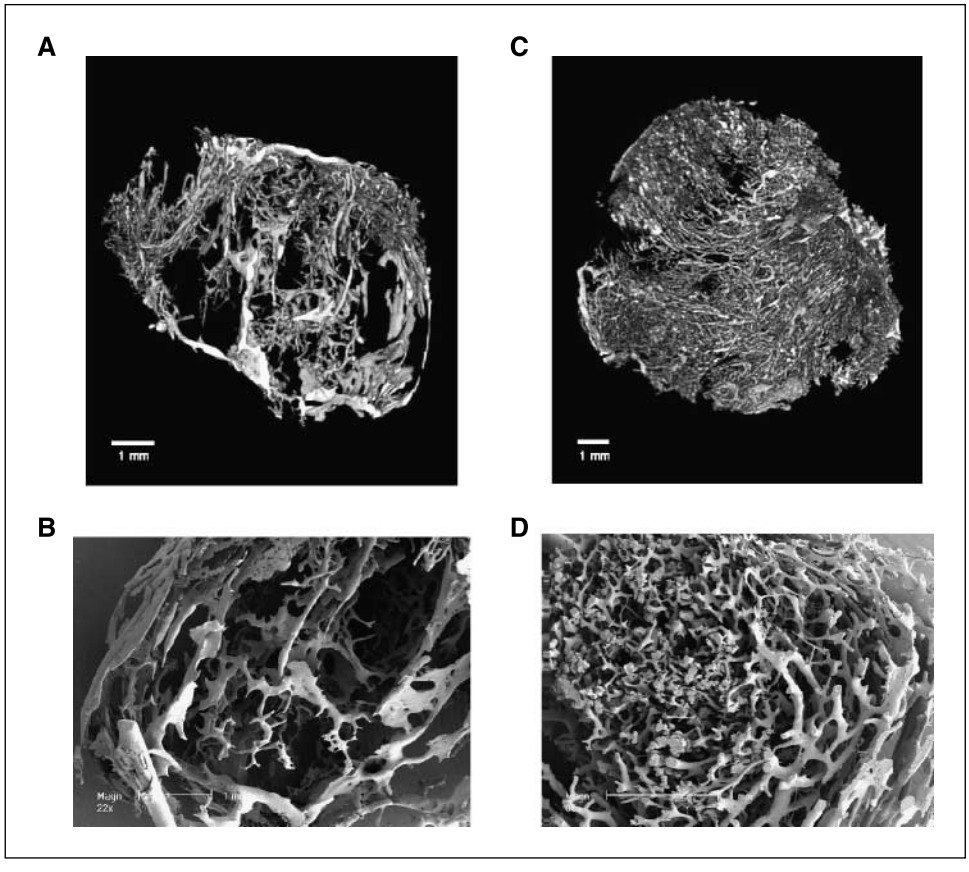

Figure 2. Three-dimensional tumor microvascular architecture as shown by corrosion casting. *A* and *C,* volume renderings from micro-CT data of whole LS174T and SW1222 tumors, respectively, showing the more patchy and heterogeneous distribution in LS174T. *B* and *D,* scanning electron micrographs showing high-power detail of vessels in LS174T and SW1222, respectively.

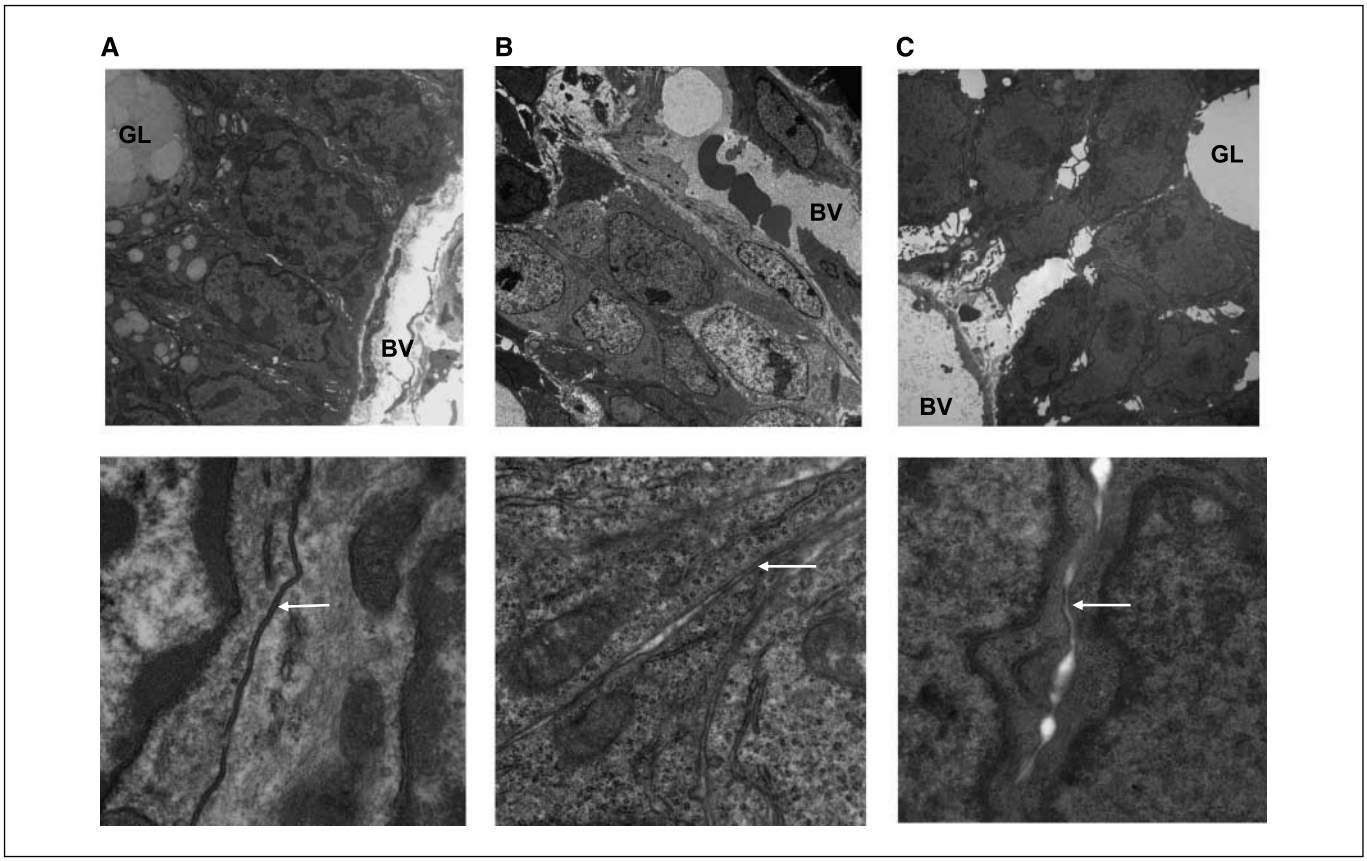

Figure 3. Transmission electron micrographs comparing the structure of normal colon and the colorectal xenografts. *A,* normal colon showing a regular pattern of epithelial cells lined up along a glandular lumen (*top*, magnification, ×5,600) and regular gap junctions (*bottom*, magnification, ×31,000). *B,* LS174T showing randomly scattered, compact tumor cells (*top*, magnification, ×4,400) and frequent gap junctions (*bottom*, magnification, ×31,000). *C,* SW1222 showing more regular tumor cells with large intercellular spaces (*top,* ×4,400) and shorter gap junctions (*bottom*, magnification, ×31,000). *BV,* blood vessel; *GL,* glandular lumen; *arrows,* gap junctions.

occasionally observed scattered throughout the tumors following i.v. injection, but localization was too low to image or quantify.

Phosphor plate image analysis studies with radiolabeled antibody. Because distribution of fluorescently labeled MOPC was difficult to observe, phosphor plate imaging studies were done on LS174T tumors from mice given radiolabeled antibody, to quantify movement over time from peripheral, viable tissue to central necrosis. Results were compared with those obtained for A5B7 in the same model. The viable to necrotic ratios achieved at time points 3, 24, and 48 h for MOPC were 0.9, 0.83, and 0.79, whereas those for A5B7 were 3.5, 2.2, and 1.5, respectively.

Discussion

We initially compared biodistribution and therapeutic efficacy of the same anti-CEA antibody, A5B7, in two human colorectal xenografts chosen to represent different clinical conditions, the LS174T being moderate to poorly differentiated, and the SW1222 being well differentiated with some resemblance to normal colon. Similar gross antibody uptake over time in the two xenografts, shown in the current study (Fig. 4*A* and *B*) and previous investigations (28, 29), did not translate into equivalent radioimmunotherapy responses with ^{131}I-labeled A5B7; the LS174T required a 3-fold increase in dose (18.0 versus 6.0 MBq) to equal the growth inhibition seen in SW1222 (Fig. 4*C* and *D*). We therefore compared tumor architecture and investigated tumor-related mechanisms that might be influencing radioimmunotherapy responses. This was achieved by using a range of high-resolution, multifluorescence microscopy systems and quantifying movement of fluorescently labeled A5B7 over time in relation to antigen and blood vessel distribution. Such detail across whole tumor sections was not achievable in most previous studies, where autoradiography was used to image antibody distribution.

A major influence on delivery and efficacy of radioimmunotherapy was vessel architecture and distribution, which differed significantly between xenografts. Immunofluorescence microscopy provided two-dimensional images of vessel distribution across entire tumor sections (Fig. 6*A* and *B*), and these were confirmed as accurate representations of whole-tumor vasculature by three-dimensional corrosion casts (Fig. 2*A* and *C*), to which they bore remarkable similarity. LS174T had relatively sparse and chaotic vessels, with a heterogeneous distribution concentrating toward the periphery and several large vessels running through the tumor. SW1222 had a more prolific and homogeneous distribution of vessels, forming a pattern (Fig. 2*D*) somewhat similar to normal colon (18). Intervessel distances, calculated from fluorescence images, were 183 and 66 μm ($P < 0.05$) for LS174T and SW1222, respectively.

The effect of these vascular differences, combined with the importance of antibody-antigen interaction, was investigated in

detail using fluorescently labeled antibody. This showed that together they played a pivotal role in therapeutic outcome for the two models. Antibody extravasation was equally rapid in LS174T and SW1222 because of the hyperpermeable nature of tumor microcirculation (30), regardless of the fact that their patterns and frequency of blood vessel distribution differed greatly. Subsequent to extravasation, however, antibody movement and retention within the two models was significantly different. In the poorly differentiated LS174T tumor, the highly heterogeneous blood supply and antigen distribution led in turn to perivascular retention of antibody, with large areas of antigen and tumor remaining untargeted (Figs. 5*A, D* and 6*A, C*). In comparison, the differentiated and highly vascularized nature of SW1222, combined with the regular distribution of CEA, resulted in a more homogeneous distribution of antibody throughout the tumor, with most antigen targeted (Figs. 5*B, D* and 6*B, D*).

This is the first study to use high-resolution multifluorescence microscopy to quantify over time the "binding site barrier" effect (Fig. 6*C* and *D*), propounded by Weinstein and his group (31–34), in which high-affinity bivalent antibody diffusion through the tumor is inhibited by the very fact of successful binding to target antigen. This frequently creates heterogeneous antibody distribution, which is generally considered detrimental to radioimmunotherapy through impaired tumor penetration (35–38). It has been reported that a minimum antibody affinity of 10^{-7} mol/L is required for tumor retention above control levels, the value for A5B7 being 7.3×10^{-10} mol/L with a slight antigen excess in the current situation (36). Our studies provide further evidence for the binding site barrier effect, as A5B7 diffusion was limited to a few cell diameters, from perfused vessel to nearest antigen, in both models (Fig. 6*C* and *D*), in agreement with results for a high-affinity anti–HER-2/*neu* antibody (36). Although our tumors had a similar range of CEA expression, which in turn produced similar gross uptake of antibody, it is apparent from the tumor growth studies that this is less important for radioimmunotherapy than distribution and availability of that antigen. In the more typical LS174T, the binding site barrier had a negative influence on radioimmunotherapy by creating patchy, perivascular antibody retention, whereas in SW1222 it became a positive advantage by creating a relatively homogeneous antibody distribution throughout the tumor. CEA has a half-life of 3 to 15 days on the cell surface (37), which is compatible with the 8-day half-life of ^{131}I. Our results are supported by other authors (38) who highlight the importance of analyzing antigen accessibility and position, rather than total antigen, in tumors with an adequate blood supply and sufficient antigen for targeting. They investigated distribution of anti-CEA antibody in four colon carcinomas, including LS174T and GS-2, the latter with a morphology resembling SW1222 and over five times the CEA content of LS174T. However, antigen in GS-2 was largely inaccessible (unlike SW1222, with wide intercellular gaps), resulting in greatly reduced antibody targeting compared with LS174T. Both this and our current study highlight the importance of investigating more than one model system when evaluating antibody-targeted therapies.

To confirm the importance of antigen-antibody interaction on motility and distribution, we compared movement of A5B7 with a

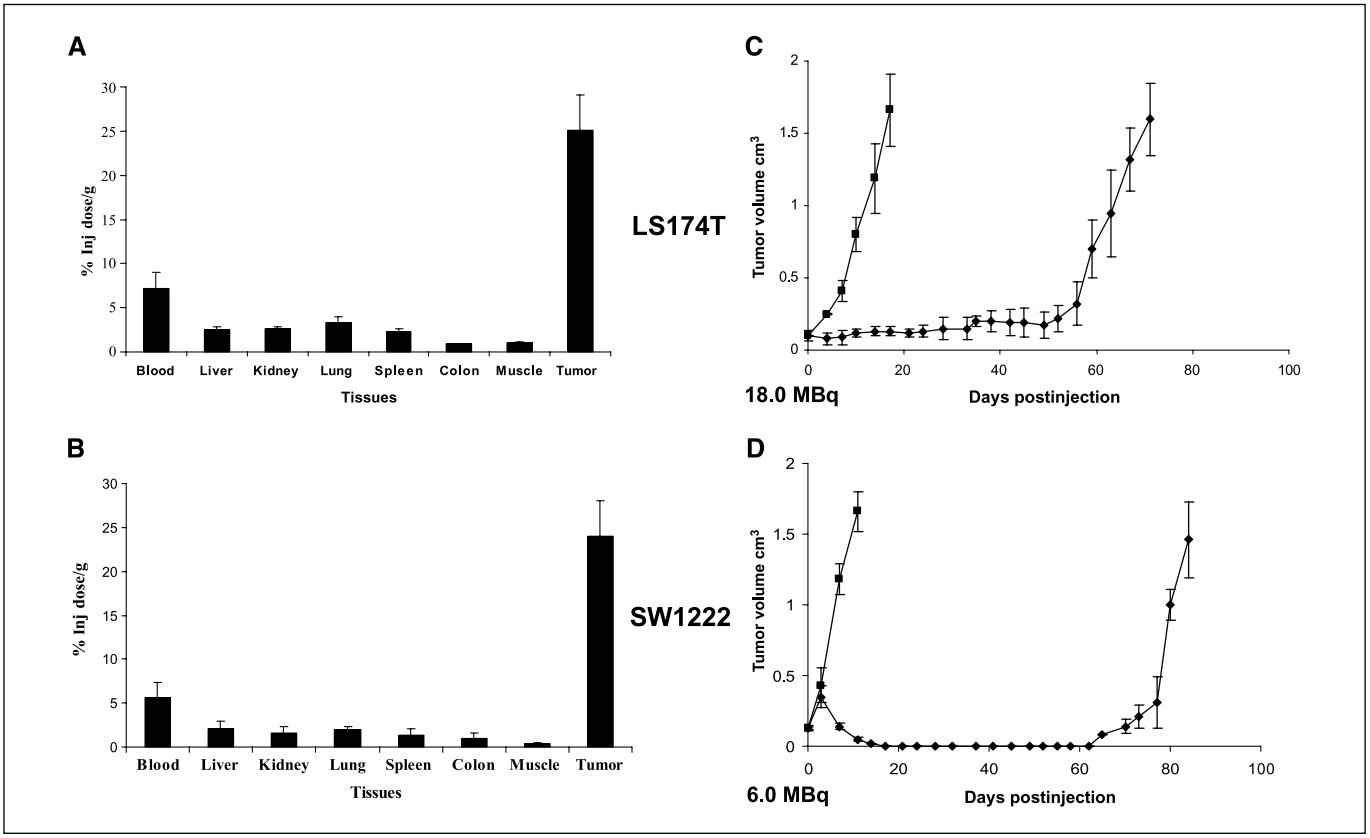

Figure 4. Distribution of A5B7 at 48 h in LS174T (*A*) and SW1222 (*B*), showing similar retention of antibody in tumor and normal tissues. Mean tumor growth following 18.0 MBq ^{131}I-labeled A5B7 in LS174T (*C*) and 6.0 MBq ^{131}I-labeled A5B7 in SW1222 (*D*), demonstrating that thrice the dose was required in LS174T for the same therapeutic effect.

nonspecific antibody. Unlike A5B7, MOPC never reached a positive tumor to blood ratio in biodistribution studies, and produced no therapeutic response when labeled with ^{131}I. Initially, we used fluorescently labeled MOPC to study motility in both models. However, low levels of localization, removal of unbound antibody during processing of frozen tumor sections (33, 34), and rapid diffusion made it impossible to image. We therefore used phosphor imaging of radiolabeled antibody and compared movement over time with A5B7 in LS174T, which showed the most obvious binding site barrier effect (Figs. 5*A, D* and 6*A*). MOPC diffused rapidly

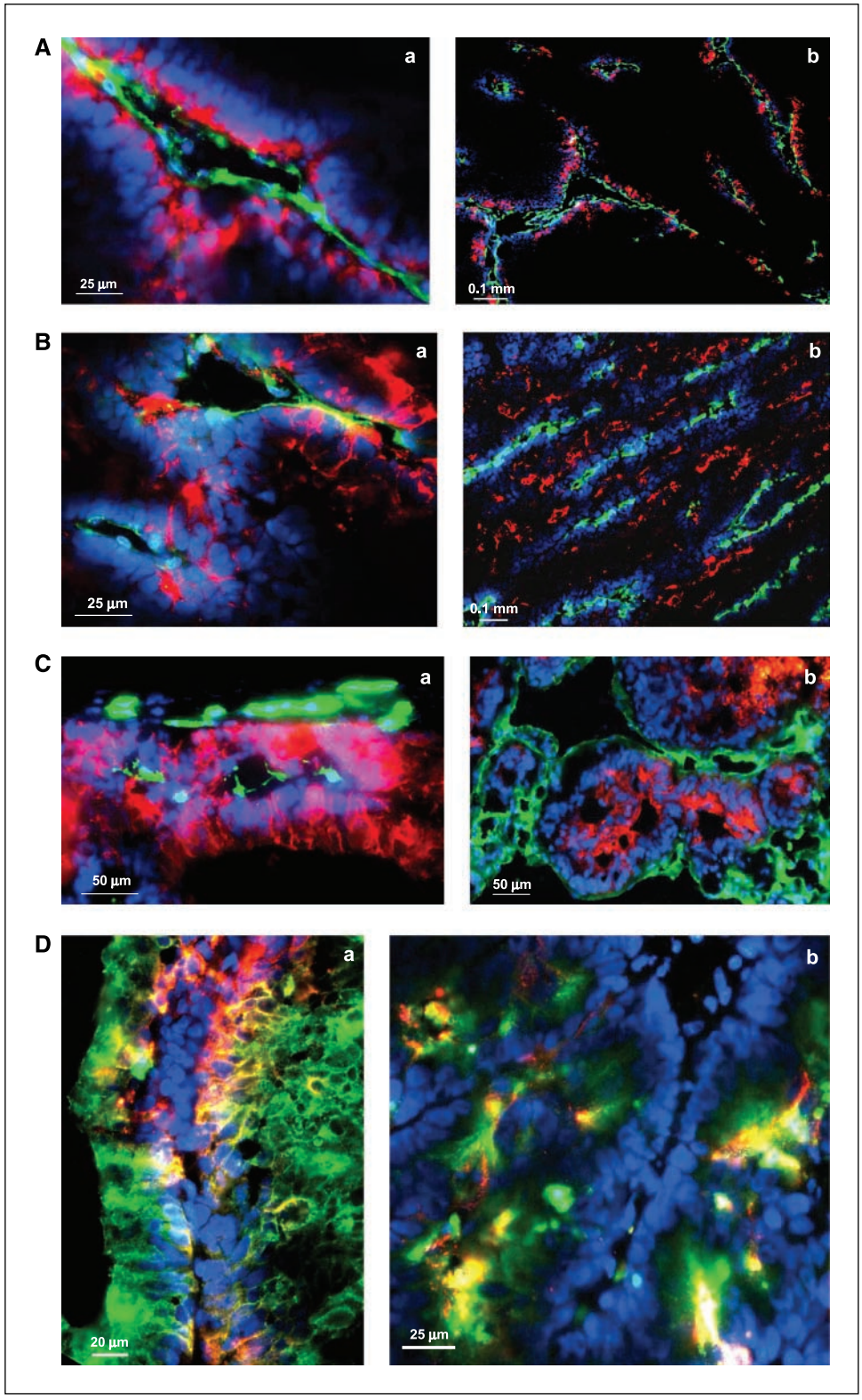

Figure 5. Immunofluorescence images showing the relationship between fluorescently labeled A5B7 distribution and tumor morphology in LS174T and SW1222 xenografts. *A,* distribution of A5B7 in LS174T at 5 min (*a*), ×40, and 1 h (*b*), ×20 montage. *B,* distribution of A5B7 in SW1222 at 5 min (*a*) ×40, and 1 h (*b*), ×20. *C,* high-power detail of antibody binding at 24 h to (*a*) perivascular tumor cells in LS174T ×40, and (*b*) luminal surface of tumor cells in SW1222 ×20. *Red,* antibody; *green,* blood vessel; *blue,* nuclei of cells adjacent to perfused vessels. *D,* antigen-antibody interaction at 1 h after antibody injection in LS174T (*a*) and SW1222 (*b*); magnification, ×40. *Red,* antibody; *green,* antigen; *yellow,* colocalization of antibody and antigen; *blue,* nuclei of cells adjacent to perfused vessels.

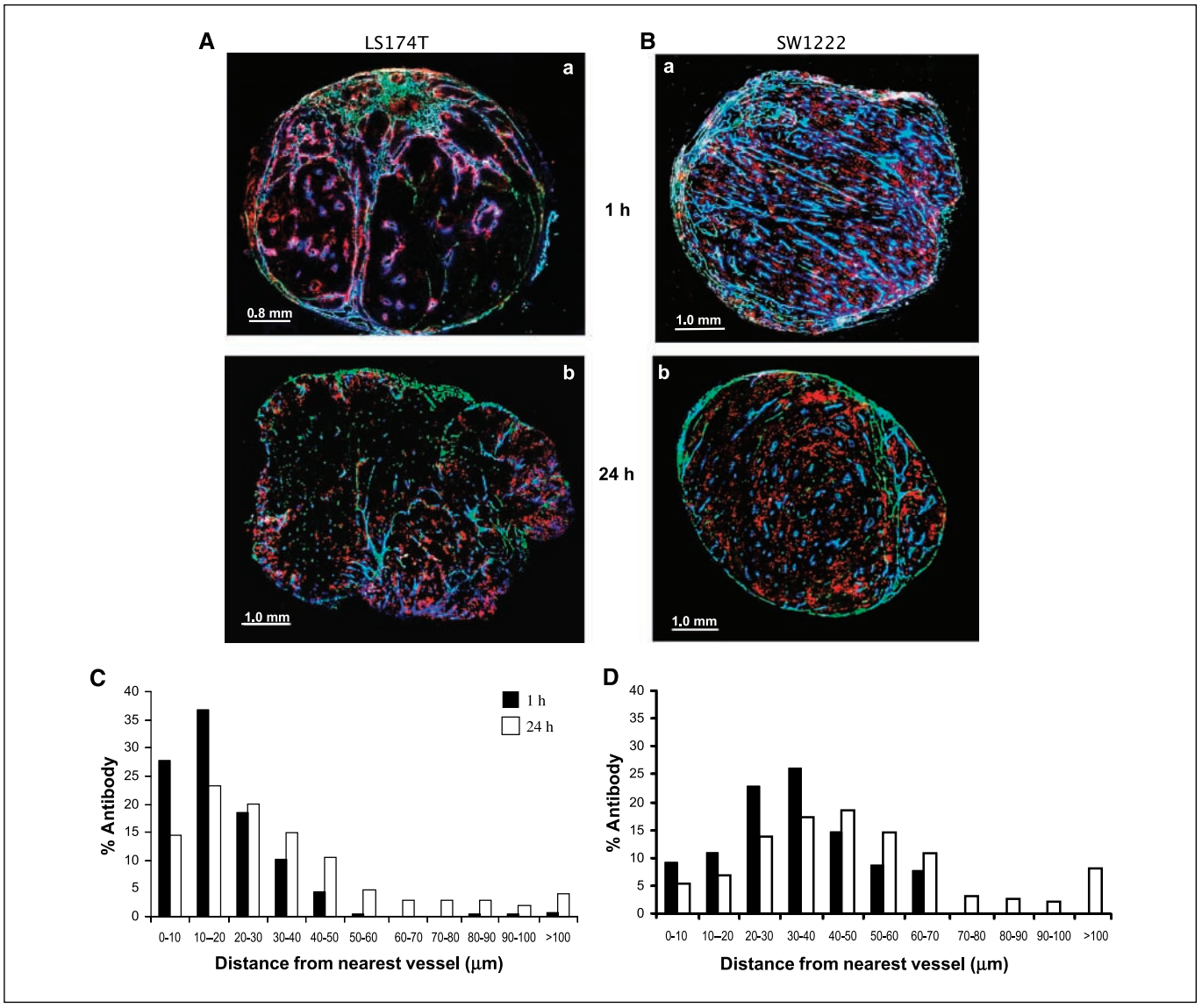

Figure 6. *A* and *B,* whole tumor sections showing distribution of A5B7 (*A*) at 1 and 24 h (×20 montage); in LS174T, the antibody remains perivascular at both 1 h (*a*) and 24 h (*b*) with a heterogeneous distribution throughout the tumor. In SW1222 (*B*), the antibody has a homogeneous distribution at both 1 h (*a*) and 24 h (*b*). Note similarity to Fig. 2*A* and *C*. *Red,* antibody; *green,* blood vessel; *blue,* nuclei of perfused cells. *C* and *D,* quantitation of antibody movement through tumors over time. Distance from the nearest blood vessel at 1 and 24 h in LS174T (*C*), showing perivascular retention and SW1222 (*D*), showing more widespread distribution.

throughout the tumor with no positive retention in viable regions, in agreement with other authors (33, 34, 36). A5B7, however, showed the importance of antigen binding, with prolonged retention in viable tumor, where it could be most effective. Our previous studies, comparing the scFv MFE23 with the mutated nonbinding version NFE, confirm that these findings also hold true for smaller antibodies; the viable to necrotic ratios at 1, 6, and 24 h were 2.2, 2.1, and 0.2 for MFE23, and 0.6, 0.4, and 0.2 for NFE (11).

A further factor that could affect antibody localization is high interstitial pressure gradient from the center to periphery of the tumor, setting up potential outward flow to create a significant barrier to antibody movement (35, 39). However, MOPC data again suggest that this is not affecting motility in the current study, but further confirm the fact that the perivascular localization of A5B7 in LS174T is mainly caused by antibody-antigen interaction (33).

Because of major differences in antibody localization and movement between the two models, we used TEM to investigate whether structural differences, in particular the presence or absence of gap junctions, could influence radioimmunotherapy. These communicating junctions, where adjacent plasma membranes are closely opposed, leave a narrow gap across which transmembrane proteins, connexins, connect one cell with another for intercellular communication, forming a potential barrier to antibody migration (33, 40). However, in spite of the differing morphologies of normal colon and the two tumor models, all contained frequent gap junctions (Fig. 3). In preliminary unpublished work, we have also shown connexin 26 in both normal colon and the two xenografts. It is therefore unlikely that gap junctions had a major effect on final antibody distribution, although the large intercellular spaces and shorter gap junctions between adjacent tumor cells in the SW1222 model

(Figs. 1*C* and 3*C*) will almost certainly speed up trans-tumor migration of antibody en route to its target antigen, and increase antigen accessibility (38).

Other parameters of our two xenografts, not investigated in the current study, are obviously involved in the outcome of radioimmunotherapy; these include hypoxia, which is extremely important but a secondary effect of global perfusion, proliferation rates (similar doubling times for LS174T and SW1222 *in vitro* of 11.9 and 12.9 h, respectively, and 3–4 days *in vivo* for both models), DNA damage response and repair efficiency following radioimmunotherapy (currently under investigation), and comparative radiosensitivity (future studies). However, others have shown that LS174T is actually more sensitive than SW1222 to a range of therapeutics *in vitro* (41). This supports the hypothesis that response to antibody-targeted therapy *in vivo* is at least as dependent on regional delivery as on the underlying genotypic/phenotypic nature of the cells, and there seems to be little doubt that tumor structure and pathophysiology played a major role in the superior response of SW1222 to radioimmunotherapy in the current study.

Data from the current and previous studies (10, 42) indicate similar localization of fluorescently and radiolabeled A5B7, and suggest that dose deposition from ^{131}I will treat most of the SW1222 tumor, but leave regions of LS174T untreated. Future studies will use the high-resolution images of antibody distribution for more accurate dosimetry modeling of therapeutic radionuclides, including dose to normoxic and hypoxic regions of viable tumor. This is particularly relevant for low-energy β and α particles, where heterogeneous antibody distribution, and therefore dose deposition, will have a larger effect on efficacy.

In conclusion, we have used fluorescently labeled antibodies and a range of digital imaging systems to show the key role played by tumor biology in antibody-targeted therapies, for two contrasting colorectal cancer models. This has facilitated accurate quantitation of antibody movement, and prediction of microregional response to therapy. It is imperative that relevant parameters are studied on the same, whole, tumor sections rather than small selected regions and/or serial sections, if antibody-tumor relationships are to be fully understood and accurately quantified. Antibody distribution and subsequent efficacy of radioimmunotherapy were principally the result of an interrelationship between three factors in the current study: distribution of blood vessels, spatial relation of antigen to these vessels, and tumor structure. Interstitial pressure and gap junctions did not seem to be major influences. Finally, results indicate that simple staining for morphology, blood vessels, and antigen distribution, across whole tumor sections, could help to predict which patients are most likely to benefit from antibody-targeted treatments, and assist in the choice of most appropriate combination therapies for treating whole tumor masses.

Acknowledgments

Received 8/2/2007; revised 10/8/2007; accepted 10/24/2007.

Grant support: Cancer Research UK (R.B. Pedley, J.L.J. Dearling, G.M. Boxer, and M.P. Robson); European Union FP6, LSHC-CT-2003-503233 STROMA (E. El Emir); National Translational Cancer Research Network (U. Qureshi); and Medical Research Council (A.A. Folarin).

The costs of publication of this article were defrayed in part by the payment of page charges. This article must therefore be hereby marked *advertisement* in accordance with 18 U.S.C. Section 1734 solely to indicate this fact.

We thank Prof. A. Mantovani for the anti-CD31 antibody and Dr. Rosalind Locke for technical assistance.

References

1. Dearling JLJ, Pedley RB. Antibody directed radionuclide therapy. In: Hoskin PJ, editor. Radiotherapy in practice: Volume III. Radioisotopes. Oxford University Press; 2007. p. 9–45.
2. DeNardo GL, Sysko VV, DeNardo S. Cure of incurable lymphoma. Int J Radiat Oncol Biol Phys 2006;66:46–56.
3. Liersch T, Meller J, Bittrich M, Krull B, Becker H, Goldenberg DM. Update of carcinoembryonic antigen radiotherapy with ^{131}I-labetuzumab after salvage resection of colorectal liver metastases: comparison of outcome to a contemporaneous control group. Ann Surg Oncol 2007;14:2577–90.
4. Sharkey RM, Goldenberg DM. Perspectives on cancer therapy with radiolabeled monoclonal antibodies. J Nucl Med 2005;46:115–27S.
5. Goldenberg DM, Sharkey RM, Paganelli G, Barbet J, Chatal J-F. Antibody pretargeting advances cancer radioimmunodetection and radioimmunotherapy. J Clin Oncol 2006;24:823–34.
6. Chatal JF, Campion L, Kraeber-Bodere F, et al. Survival improvement in patients with medullary thyroid carcinoma who undergo pretargeted anti-carcinoembryonic-antigen radioimmunotherapy: a collaborative study with the French endocrine tumor group. J Clin Oncol 2006;24:1705–11.
7. Napier MP, Begent RHJ. Radioimmunotherapy of gastrointestinal cancer. In: Riva T, editor. Cancer radioimmunotherapy. Boston: Harwood Academia; 1998. p. 333–88.
8. Flynn AA, Pedley RB, Green AJ, et al. Effectiveness of radiolabeled antibodies for radioimmunotherapy in a colorectal xenograft model: a comparative study using the linear-quadratic formulation. Int J Radiat Biol 2001; 77:507–17.
9. Flynn AA, Green AJ, Pedley RB, Boxer GM, Boden R, Begent RHJ. A mouse model for calculating the absorbed β dose, from ^{131}I and ^{90}Y labelled immunoconjugates, including a method for dealing with heterogeneity in kidney and tumor. Radiat Res 2001; 156:28–35.
10. Flynn AA, Pedley RB, Green AJ, et al. Antibody and radionuclide characteristics can enhance the effectiveness of radioimmunotherapy by selective dose delivery to radiosensitive areas of tumor. Int J Radiat Biol 2002; 78:407–15.
11. Flynn AA, Green AJ, Pedley RB, et al. A model-based approach for the optimization of radioimmunotherapy through antibody design and radionuclide selection. Cancer 2002;94:1249–57.
12. Pedley RB, Hill SA, Boxer GM, et al. Eradication of colorectal xenografts by combined radioimmunotherapy and combretastatin A4-phosphate. Cancer Res 2001;61: 4716–22.
13. Pedley RB, El-Emir E, Flynn AA, et al. Synergy between vascular targeting agents and antibody-directed therapy. Int J Radiat Oncol Biol Phys 2002;54:1524–31.
14. El Emir E, Boxer GM, Petrie IA, et al. Tumor parameters affected by combretastatin A-4 phosphate therapy in a human colorectal xenograft model in nude mice. Eur J Cancer 2005;41:799–806.
15. Yuan F, Dellian M, Fukumura D et al. Vascular permeability in a human tumor xenograft: molecular size dependence and cutoff size. Cancer Res 1995;55: 3752–6.
16. Jain RK. The next frontier of molecular medicine: delivery of therapeutics. Nat Med 1998;4:655–7.
17. Boxer G, Stuart-Smith S, Flynn A, Begent R. Radioimmunoluminography: a tool for relating tissue antigen concentration to clinical outcome. Br J Cancer 1999;80: 922–6.
18. Konerding MA, Malkusch W, Klapthor B, et al. Evidence for characteristic vascular patterns in solid tumors: quantitative studies using corrosion casts. Br J Cancer 1999;80:724–32.
19. Lane DM, Eagle KF, Begent RHJ, et al. Radioimmunotherapy of metastatic colorectal tumors with iodine-131-labelled antibody to carcinoembryonic antigen: phase I/II study with comparative biodistribution of intact and F(ab')$_2$, antibodies. Br J Cancer 1994;70: 521–5.
20. Casey JL, Napier MP, King DJ, et al. Tumor targeting of humanised cross-linked divalent-fab′ antibody fragments: a clinical phase I/II study. Br J Cancer 2002;86: 1401–10.
21. Looney WB, Mayo AA, Allen PM, et al. A mathematical evaluation of tumor growth curves in rapid, intermediate and slow growing rat hepatoma. Br J Cancer 1973;27:341–4.
22. Flynn AA, Green AJ, Boxer GM, et al. A novel technique, using radioluminography, for the measurement of radiolabeled antibody distribution in a colorectal cancer xenograft model. Int J Radiat Oncol Biol Phys 1999;43:183–9.
23. Flynn AA, Boxer GM, Begent RHJ, Pedley RB. Relationship between tumor morphology, antigen and antibody distribution measured by fusion of digital phosphor and photographic images. Cancer Immunol Immunother 2001;50:77–81.
24. Flynn AA, Pedley RB, Green AJ, et al. Optimising radioimmunotherapy by matching dose distribution with tumor structure using 3D reconstructions of serial images. Cancer Biother Radiopharm 2002;16: 391–400.
25. El-Emir E, Dearling JLJ, Huhalov A, et al. Characterisation and radioimmunotherapy of L19-SIP, an anti-angiogenic antibody against the extra domain B of fibronectin, in colorectal tumor models. Br J Cancer 2007;96:1862–70.

26. Sharma SK, Pedley RB, Bhatia J, et al. Sustained tumor regression of human colorectal cancer xenografts using a multifunctional mannosylated fusion protein in antibody directed enzyme prodrug therapy (ADEPT). Clin Cancer Res 2005;11:814–25.

27. Lee E, Desu M. A computer program for comparing K samples with right censored data. Computer Prog Biomed 1972;2:315–21.

28. Pedley RB, Begent RHJ, Boden JA, Boxer GM, Boden R, Keep PA. Enhancement of radioimmunotherapy by drugs modifying tumour blood flow in a colonic xenograft model. Int J Cancer 1994;57:830–5.

29. Lankester KJ, Maxwell RJ, Pedley RB, et al. Combretastatin A-4-phosphate effectively increases tumor retention of the therapeutic antibody, ^{131}I-A5B7, even at doses that are sub-optimal for vascular shut-down. Int J Oncol 2007;30:453–60.

30. Hobbs SK, Monsky WL, Yuan F, et al. Regulation of transport pathways in tumor vessels: role of tumor type and microenvironment. Proc Natl Acad Sci U S A 1998; 95:4607–12.

31. Fujimori K, Covell DG, Fletcher JE, Weinstein JN. A model analysis of monoclonal antibody percolation through tumors: a binding site barrier. J Nucl Med 1990; 31:1191–8.

32. Van Osdol W, Fujimori K, Weinstein JN. An analysis of monoclonal antibody distribution in microscopic tumor nodules: consequences of a 'binding site barrier'. Cancer Res 1991;51:4776–84.

33. Juweid M, Neumann R, Paik C, et al. Micropharmacology of monoclonal antibodies in solid tumors: direct experimental evidence for a binding site barrier. Cancer Res 1992;52:5144–53.

34. Saga T, Neumann RD, Heya T, et al. Targeting cancer micrometastases with monoclonal antibodies: a binding site barrier. Proc Natl Acad Sci U S A 1995;92: 8999–9003.

35. Nielsen UB, Adams GP, Weiner LM, Marks JD. Targeting of bivalent anti-ErbB2 antibody fragments to tumor cells is independent of the intrinsic antibody affinity. Cancer Res 2000;60:6434–40.

36. Adams GP, Schier R, McCall AM, et al. High affinity restricts the localization and tumor penetration of single-chain Fv antibody molecules. Cancer Res 2001;61:4750–5.

37. Graff CP, Wittrup KD. Theoretical analysis of antibody targeting of tumor spheroids: importance of dosage for penetration, and affinity for retention. Cancer Res 2003;63:1288–96.

38. Blumenthal RD, Sharkey RM, Kashi R, Natale AM, Goldenberg DM. Physiological factors influencing radioantibody uptake: a study of four human colonic carcinomas. Int J Cancer 1992;51:935–41.

39. Jain RK, Baxter LT. Mechanisms of heterogeneous distribution of monoclonal antibodies and other macromolecules in tumors: significance of elevated interstitial pressure. Cancer Res 1988;48:7022–32.

40. Kamibayashi Y, Oyamada Y, Mori M, Oyamada M. Aberrant expression of gap junction proteins (connexins) is associated with tumor progression during multistage mouse skin carcinogenesis *in vivo*. Carcinogenesis 1995;16:1287–97.

41. Buda A, Qualtrough D, Jepson MA, Martines D, Paraskeva C, Pignatelli M. Butyrate downregulates $\alpha(2)\beta(1)$ integrin: a possible role in the induction of apoptosis in colorectal cancer cell lines. Gut 2003;52:729–34.

42. Pedley RB, Boden JA, Boden R, et al. Ablation of colorectal xenografts with combined radioimmunotherapy and tumour blood flow modifying agents. Cancer Res 1996;56:3293–300.